Supplementary Information

Assembly of Cerium-Based Coordination Polymer into Variant Polycrystalline 2D-3D CeO_{2-x} Nanostructures

Sajjad S. Mofarah *[a], Esmaeil Adabifiroozjaei[b], Yuan Wang[c], Hamidreza Arandiyan[d], Raheleh Pardehkhorram[c], Yin Yao[e], M. Hussein N. Assadi[a,f], Rashid Mehmood[a,g], Wen-Fan Chen[a,h], Constantine Tsounis[i], Jason Scott[i], Sean Lim[e], Richard Webster[e], Vicki Zhong[a], Yuwen Xu[a], Pramod Koshy[a], and Charles C. Sorrell[a]

[a]School of Materials Science and Engineering, UNSW Sydney, Sydney, NSW 2052, Australia. Email: s.seifimofarah@unsw.edu.au
[b]Research Center for Functional Materials (RCFM), National Institute for Materials Science (NIMS), Tsukuba, Ibaraki 305-0047, Japan
[c]School of Chemistry, UNSW Sydney, Sydney, NSW 2052, Australia
[d]Laboratory of Advanced Catalysis for Sustainability, School of Chemistry, The University of Sydney, Sydney 2006, Australia
[e]Electron Microscopy Unit (EMU), Mark Wainwright Analytical Centre, UNSW Sydney, Sydney, NSW 2052, Australia
[f]Center for Green Research on Energy and Environmental Materials (GREEN), National Institute for Materials Science (NIMS), 1-1 Namiki, Tsukuba, Ibaraki 305-0044, Japan
[g]Department of Physics and Astronomy, ARC Centre of Excellence for Nanoscale BioPhotonics, Macquarie University, Sydney, NSW 2109, Australia
[h]Institute of Medical Science and Technology, National Sun Yat-sen University, Kaohsiung 80424, Taiwan
[i]Particles and Catalysis Research Group, School of Chemical Engineering, UNSW, Sydney, NSW 2052, Australia.

*Corresponding author. Email: s.seifimofarah@unsw.edu.au

Synthesis procedure: Formation mechanism

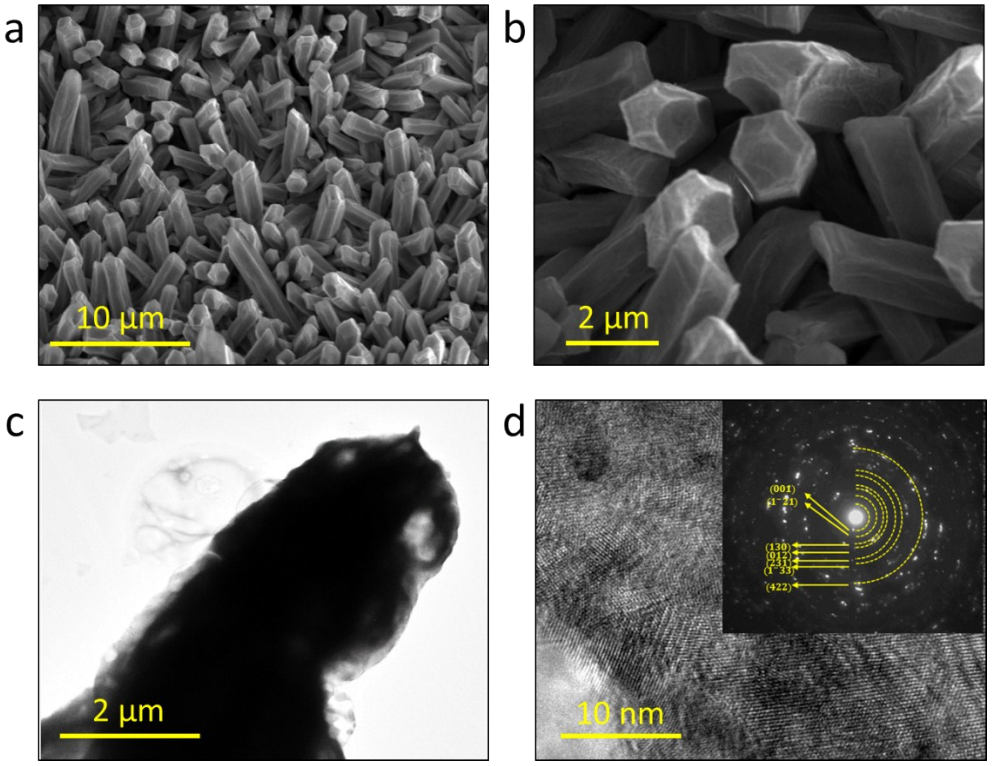

Fig. S1 (a,b) SEM and (c,d) TEM images of Ce-CP structure (inset shows respective SAED pattern)

The Ce-CP rods were synthesised under anodic electrochemical current at an aqueous solution and within the oxygen evolution region. The reason to make such a unique atmosphere is rationalised through thermodynamic behaviour of cerium (Ce) species in aqueous solution. To be clarified, the newly revised Pourbaix diagram for Ce^{3+}-Ce^{4+}-TCA-H_2O is shown in Fig. S2.

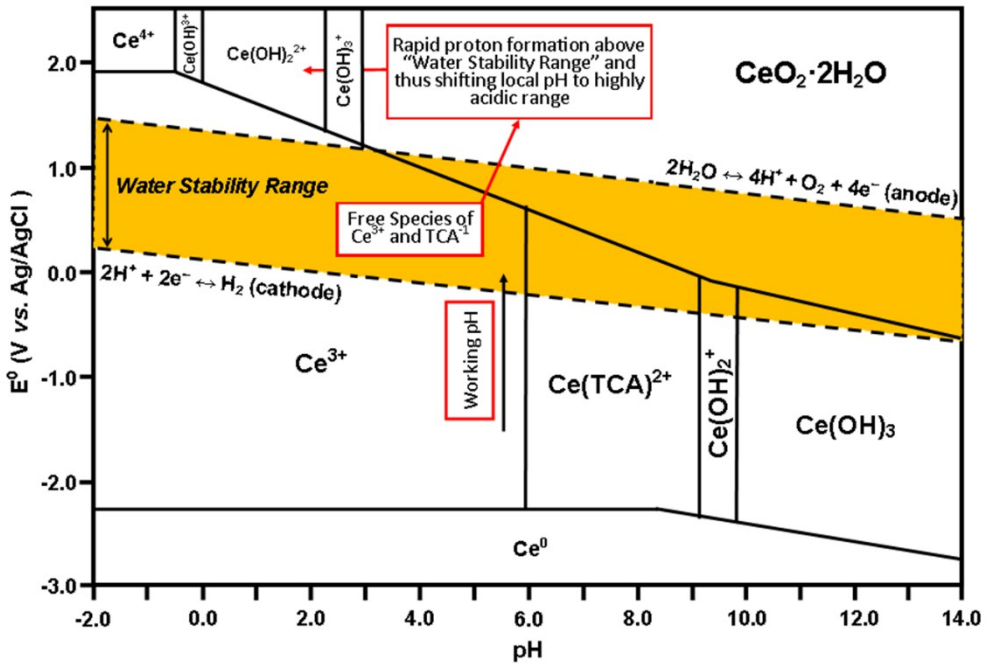

Fig. S2 Pourbaix diagram for the system Ce^{3+}-Ce^{4+}-H_2O-TCA, showing the pathway for modified anodic chronopotentiometric electrodeposition (MACE).

The possible chemical reaction towards the formation of Ce-CP are as follows:

1. Deprotonation of TCA in water followed by dropping in pH value from 6.5 to <2.3:

$$CCl_3COOH + H_2O \rightarrow H_3O^+ + CCl_3COO^- \qquad \text{Equation 1}$$

2. Dissociation of cerium nitrate salt in the solution resulting in the release of free Ce^{3+} and nitrate anions:

$$Ce(NO_3)_3 \cdot 6H_2O \rightarrow Ce^{3+} + 3NO_3^- + 6H_2O \qquad \text{Equation 2}$$

3. At pH = 6, the oxidation voltage for cerium was found to be 0.55 V vs. Ag/AgCl, while the onset of water oxidation is laid at 0.8 V. Applying constant potential of 1.2 V vs. Ag/.AgCl caused a rapid generation of oxygen at the anode (FTO) surface (Equations 3-5):

$$2H_2O \rightarrow 4H^+ + O_2 + 4e^- \qquad \text{Equation 3}$$

$$4OH^- \rightarrow 4H^+ + 2O_2 + 4e^-$$ Equation 4

$$HO_2^- + OH^- \rightarrow H_2O + O_2 + 2e^-$$ Equation 5

The high production rate of oxygen molecules on the FTO substrate results in oxidation of Ce(III) species to Ce(IV). However, during water oxidation, the evolution of one-mole oxygen is followed by the formation of 4 mole protons that in turn results in a rapid drop in local pH and an increased concentration of protons. At this condition, Ce(IV) hydroxide species are in soluble form. Additionally, owing to low pK_a value of the TCA, deprotonated TCA acted as secondary building units (SBUs), bridging Ce(IV) hydroxide species together resulting in the formation of a novel polycrystalline Ce-CP. The corresponding equation is given below:

$$Ce^{4+} + 2OH^- + 2TCA + 2H_2O = Ce(OH)_2(TCA)_2 \cdot 2H_2O$$ Equation 6

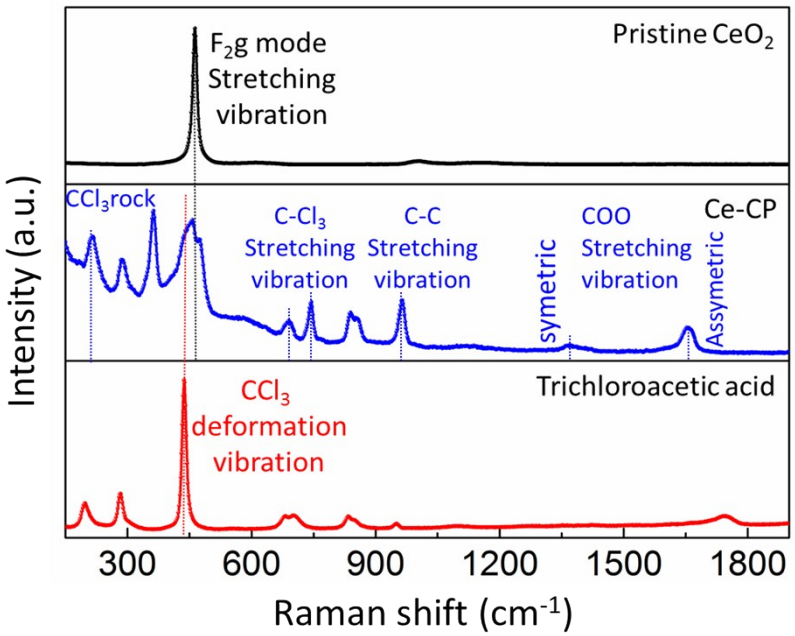

Fig. S3 Raman spectra of Ce-CP tube (top) and TCA (bottom).

Raman data: The Raman spectra of the Ce-CP was analysed comprehensively and indexed according to the vibrational modes of pure TCA and CeO_2, as explained below:

Most of the TCA peaks are present in Ce-CP rods indicating the presence of TCA molecule in the structure. The peak at 214 cm^{-1} is ascribed to the CCl_3 rock.[1] The peaks centred at 288 is assigned

to the symmetric deformation of CCl_3,[2] while the peak at 430 cm^{-1} is attributed to the asymmetric bending vibrations of the C-Cl_3 bond.[3] Additionally, the symmetric stretching vibrations of C-Cl_3 bond in TCA delivers a peak at 688 cm^{-1}, while the peaks for asymmetrical stretching of the C-Cl_3 bond appear at 845 and 744 cm^{-1}.[3] The peak positioned at 952 cm^{-1} corresponds to the symmetric stretching vibration mode of the carbon-carbon bond (C-C).[2] Further comparison of the two spectra shows that Raman shifts occurred in some of the peaks (952 cm^{-1} to 962 cm^{-1}, 700 cm^{-1} to 740 cm^{-1}, and 683 cm^{-1} to 688 cm^{-1}), which are attributed to the alteration in vibrational modes of the TCA bonds owing to their interactions with Ce ions.[4] Furthermore, the peak at 1746 cm^{-1} for TCA, which is attributed to the stretching vibrations of COO^-, is split into two peaks at 1367 and 1662 cm^{-1} for the Ce-CP spectra.[4] The splitting can result from the bonding between the COO^- group of TCA and Ce cations followed by corresponding symmetric (1367 cm^{-1}) and asymmetric (1662 cm^{-1}) vibrations. This is confirmed by revealing the peak at 455 cm^{-1}, which is close to the symmetric vibration of Ce and eight coordinated oxygen.[5, 6]

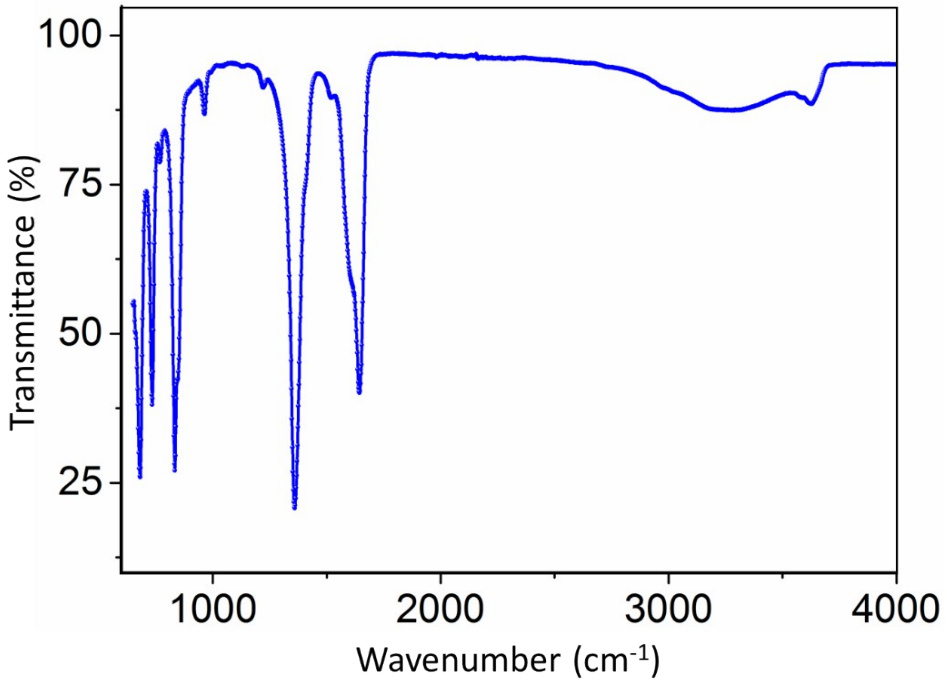

Fig. S4 FTIR spectra of Ce-CP tubes.

FTIR data: The bands centred at ~3600 and ~3400 cm^{-1} show stretching vibrations of hydroxyl groups revealing the presence of water and OH group in the Ce-CP.[4] The peaks at ~1600 and ~1360 cm^{-1} are attributed to the asymmetric and symmetric stretching vibrations of carboxylic groups that is bonded to Ce cations. Also, the peaks at 1030 cm^{-1} and ~960 cm^{-1} are assigned to bending

vibration of COO^- and symmetric vibration of C-C, respectively.[7] Similar to Raman spectra, the peaks at 688, 744, and 845 cm^{-1} are attributed to C-Cl_3 vibration modes.

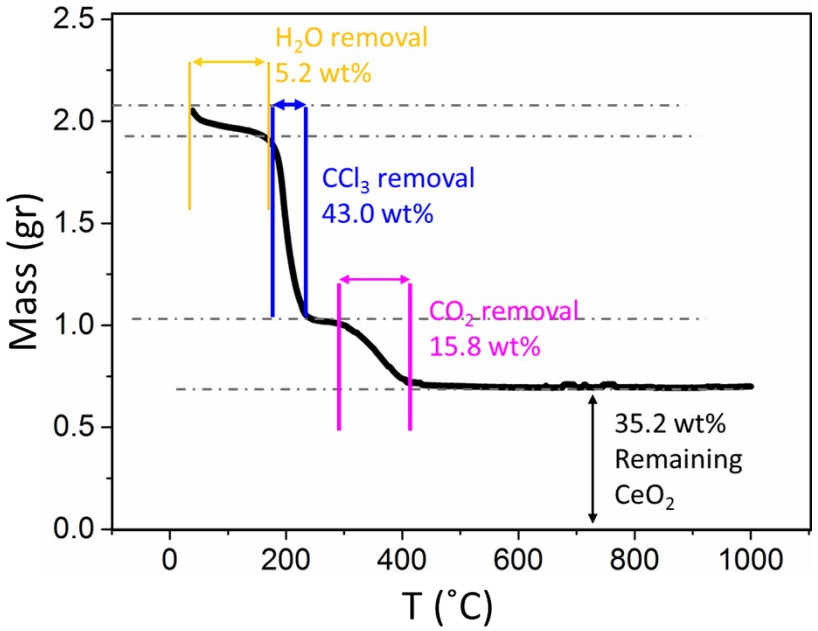

Fig. S5 TGA analysis of Ce-CP in a nitrogen atmosphere.

TGA data: TGA analysis of Ce-CP under reducing nitrogen atmosphere illustrates three steps involving removal of structural water (5.2% at ~160˚C), carbon chloride (43.0% at ~220˚C), and CO_2 (15.8% at ~420˚C) from the Ce-CP, respectively. At temperature above 420˚C, the remaining Ce-CP (35.2 wt%) transforms into CeO_2.

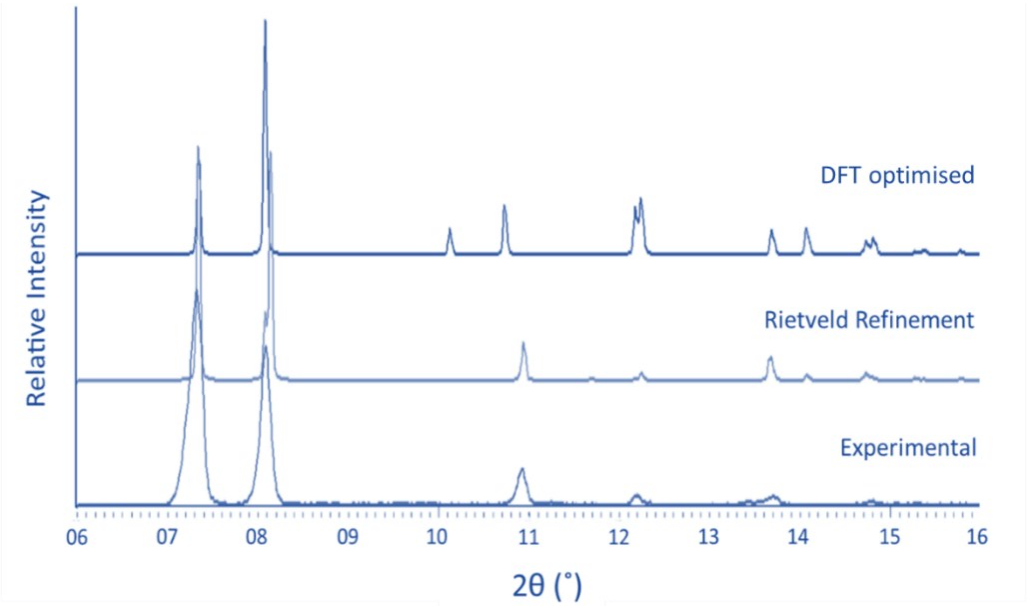

Fig. S6 The experimental, refined and simulated XRD patterns.[8]

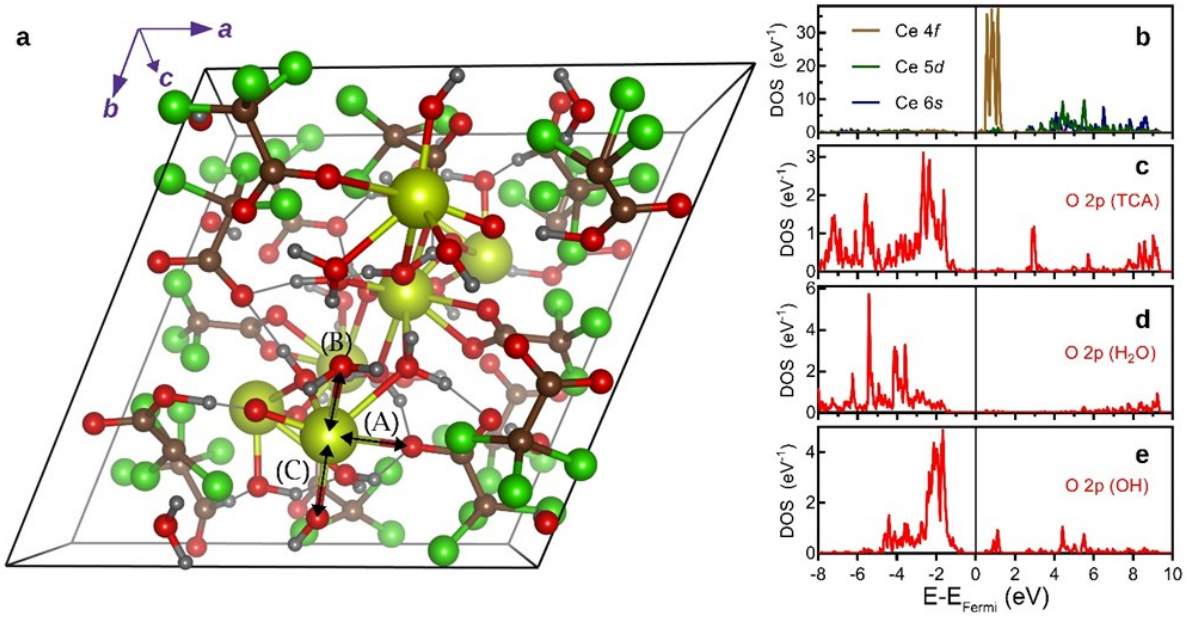

Fig. S7 (a) The relaxed Ce-CP structure commensurate with experimental lattice parameters. All TCA molecules were found to remain intact. A, B, and C denote the Ce ion bonding to a TCA molecule, a water molecule and an OH group respectively. (b)-(e) show the site projected partial density of states of the marked Ce ion and the O ions from distinct coordinating ligands.

Since XRD cannot identify the position of lighter atoms such as H with great accuracy, a full geometry optimisation was performed on the experimentally refined structure. The final optimised structure which is shown in Fig. S7a reproduces the main diffraction peaks at low angles centered at 7.34982° and 813390° with reasonable accuracy. It should be noted factors such as the low resolution of the XRD measurement, supercell approach of the density functional calculations and the fact that the simulation corresponds to 0 K condition limit greater match between theory and experiment.

Furthermore, the Ce-$O_{(TCA)}$ bond was found to be ~ 2.56 Å which was longer than both Ce-$O_{(H2O)}$ bond at ~2.60 Å and Ce-$O_{(OH)}$ bond at 1.96 Å. The longer Ce-$O_{(TCA)}$ bond length reinforces the notion of the fragility of this bond. The empty Ce 4f, 5d and 6s states, in Fig. 7b, point to a 4+ oxidation state for Ce ions. Moreover, the lack of any overlap between Ce states and coordinating O states (Fig. 7(b)-(e)) indicates lack of any strong covalent bonding to Ce.

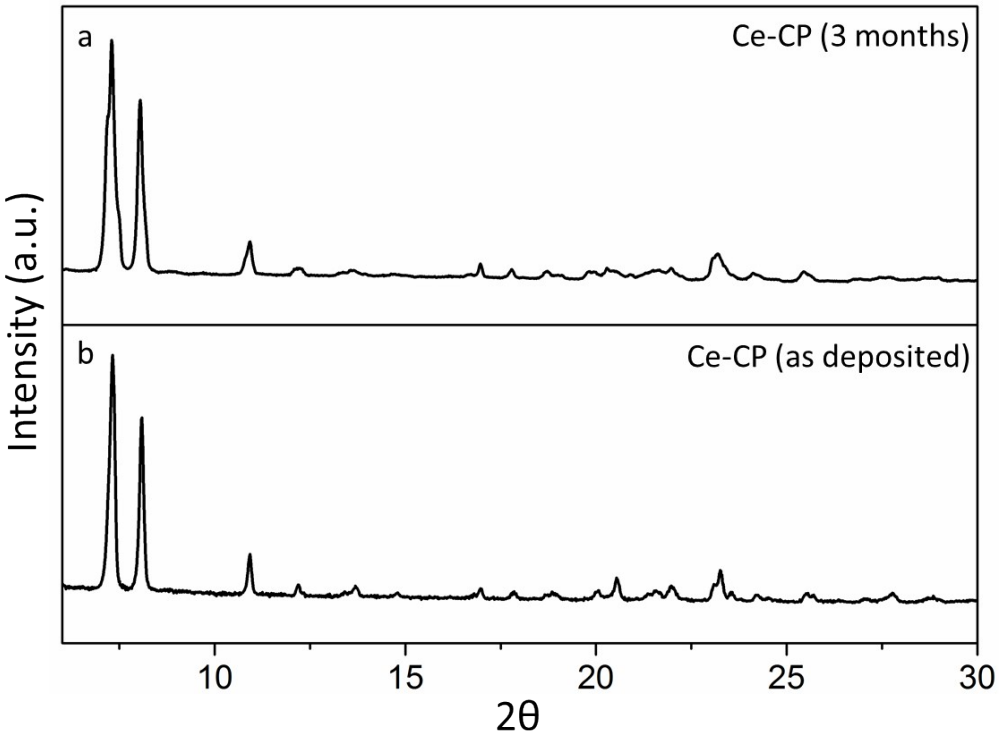

Fig. S8 Experimental X-ray pattern obtained from (a) freshly prepared Ce-CP and (b) aged sample (under ambient condition) for 3 months.

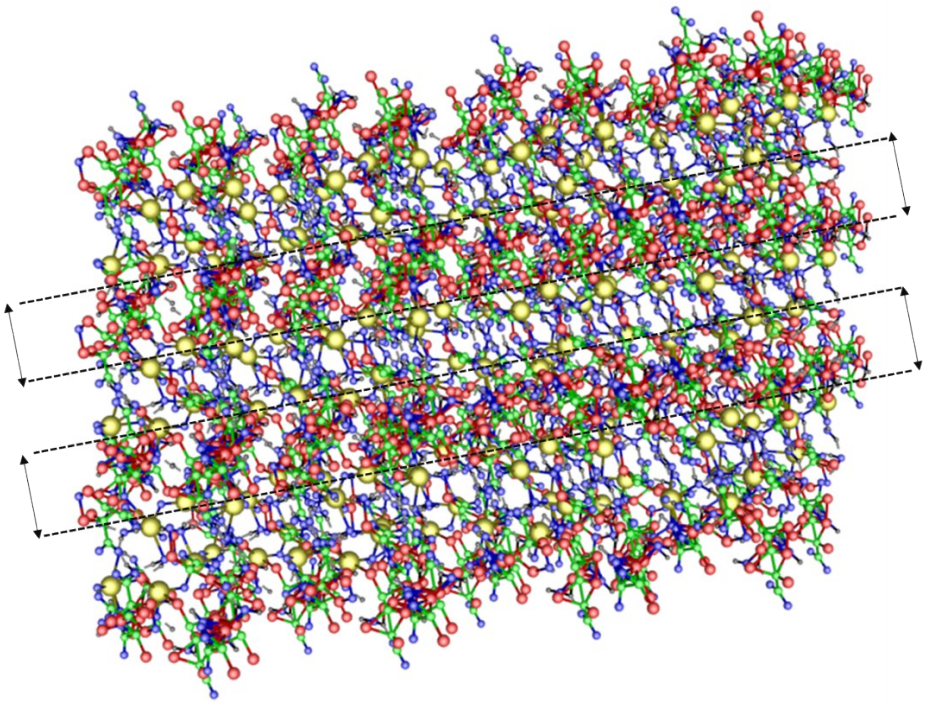

Fig. S9 Schematic of stratified (layered) structure of Ce-CP. Large yellow spheres = Ce^{4+}, small green spheres = C^{4+}, small black sphere = H^{+}, small blue spheres = O^{2-}, small red spheres = Cl^{-}.

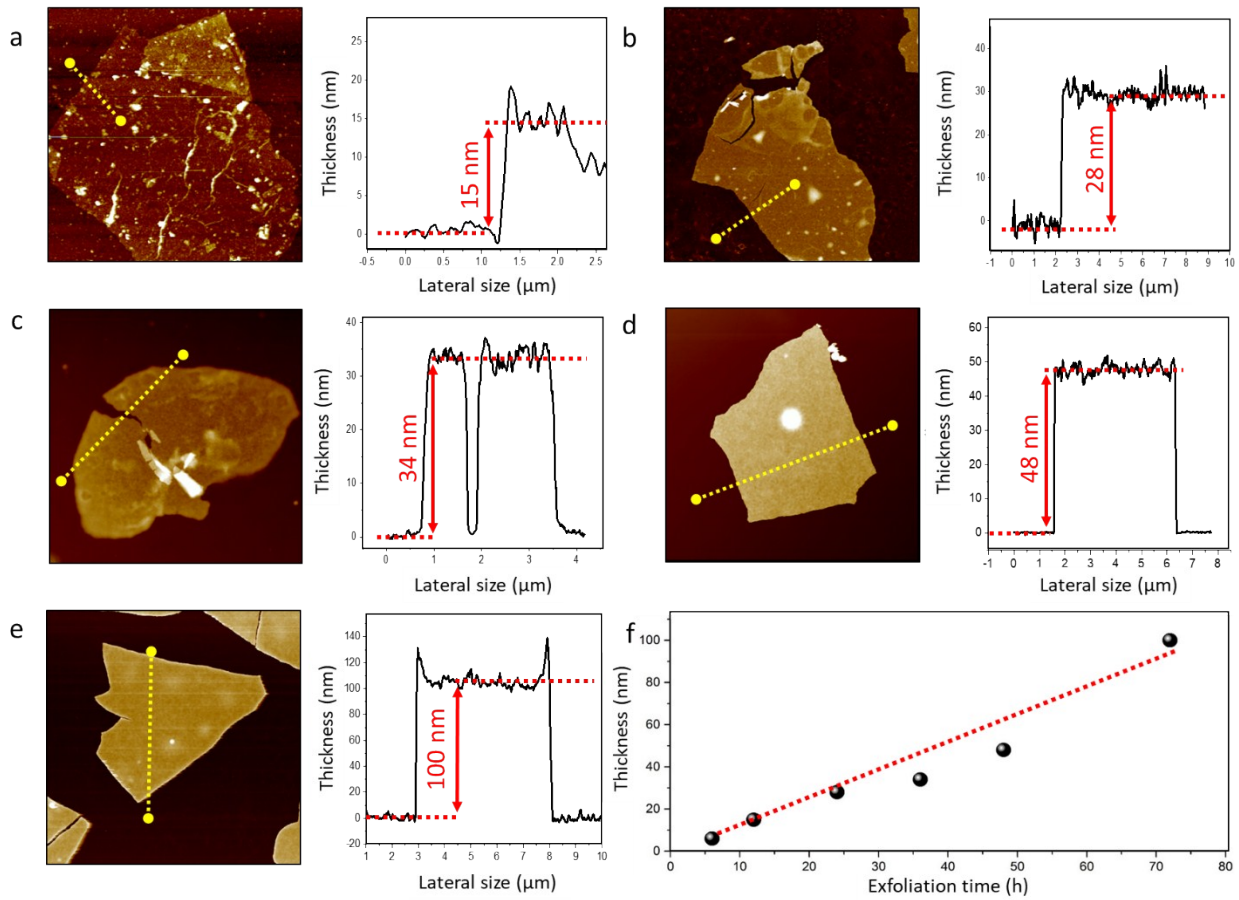

Fig. S10 AFM image and corresponding height profile of Ce-CP nanosheets printed from surface of ethanol at evaporation times of (a) 12 h, (b) 24 h (c) 36 h (d) 48 h, and (e) 72 hours, (f) Plot of Ce-CP nanosheet thickness variations against exfoliation (touch printing) time.

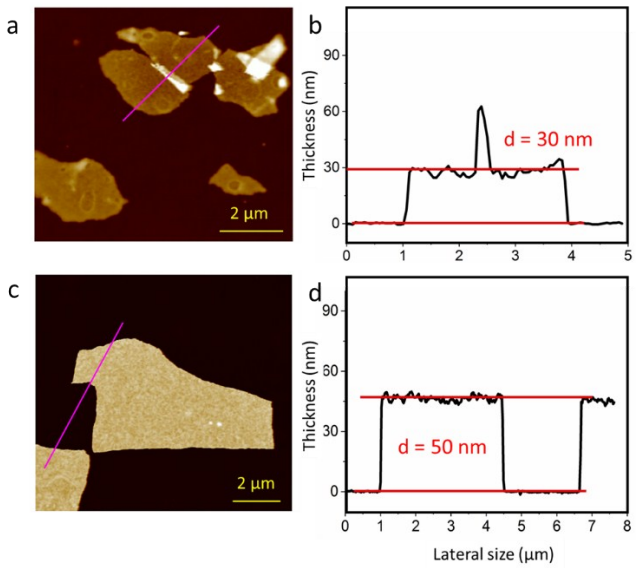

Fig. S11 AFM image and corresponding height profile of Ce-CP nanosheets printed from surface of ethanol at different Ce-CP concentration of (a,b) 4 M, (c,d) 8 M.

Recrystallisation Ce-CP from ethanol: Disassembly/reassembly of the Ce-CP resulted in no considerable change in crystal and chemical structures. To confirm, XRD, Raman, HRTEM, Raman, and FTIR data of the Ce-CP rod and re-assembled Ce-CP upon ethanol evaporation were studied, as shown in Fig. S12.

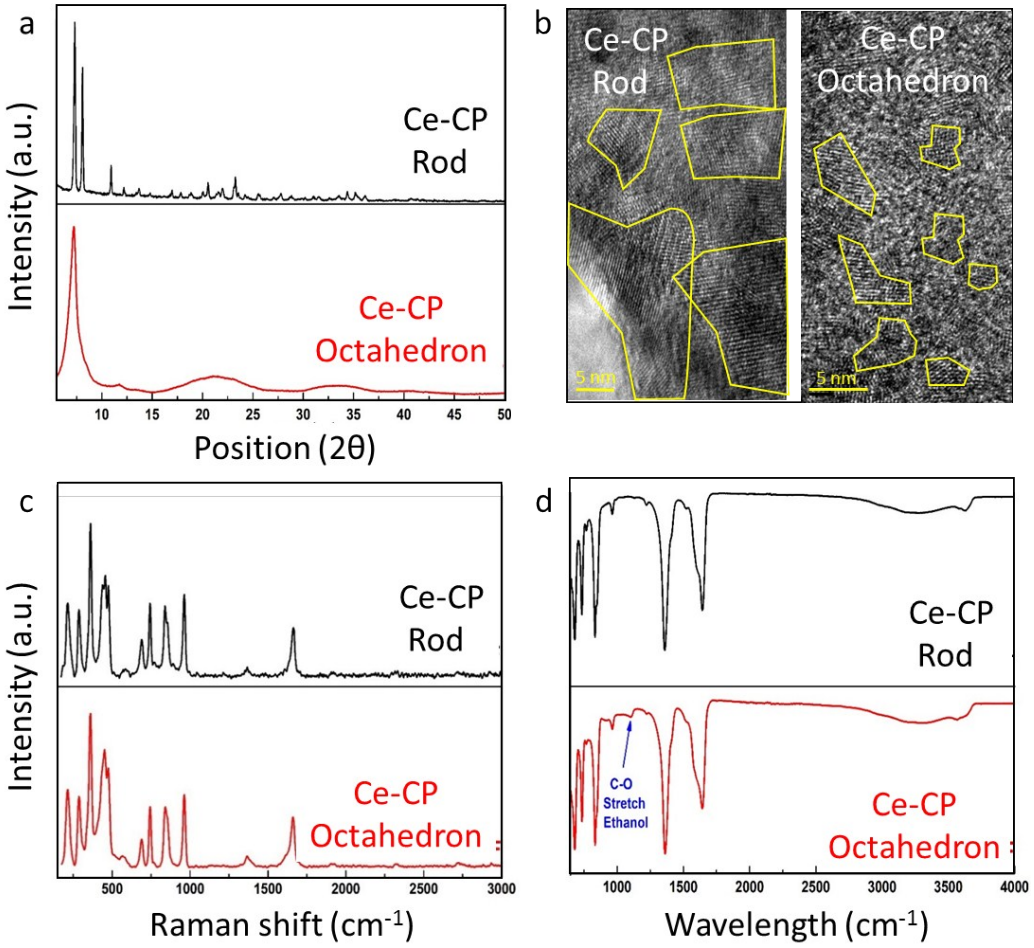

Fig. S12 (a) XRD patterns of Ce-CP rod synthesised by electrochemical deposition (black) and Ce-CP octahedron obtained by dissolution/recrystallisation method in ethanol (red), (b) HRTEM image of Ce-CP rod (left) and Ce-CP octahedron (enclosed regions by yellow solid line show single crystallites, (c) Raman spectra of Ce-CP rod (black) and Ce-CP octahedron (red), and (d) Fourier transform IR (FTIR) spectra of Ce-CP rod (black) and Ce-CP octahedron (red).

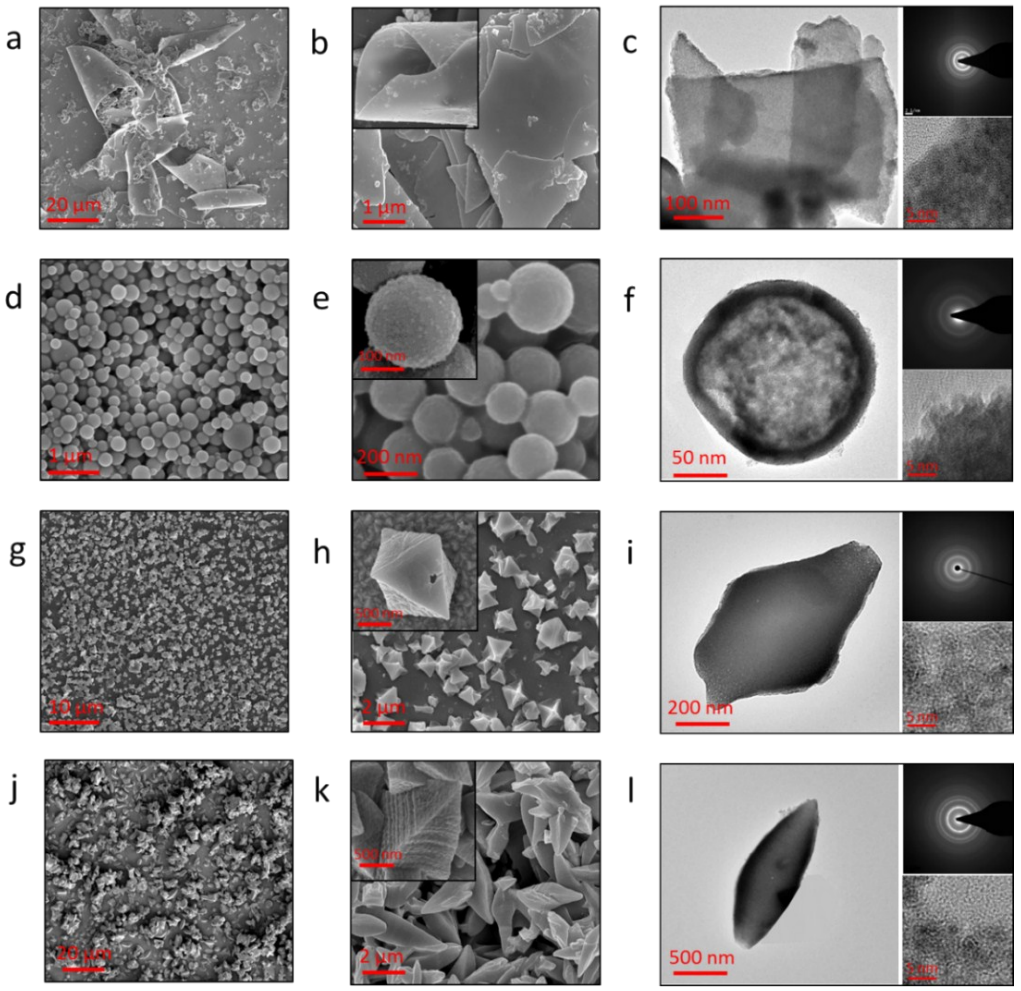

Fig. S13 SEM, TEM, HRTEM images and SAED pattern of CeO_{2-x} derived from Ce-CP morphologies synthesized at 0°C: (a-c) 4 M, and at 25°C: (d-f) 4 M, (g-i) 8 M, and (j-l) 120 M.

Surface characterisation of derived CeO_{2-x}

To quantify the $[V_O^{\bullet\bullet}]$ from XPS results, atomic percentages of both Ce^{3+} and Ce^{4+} were determined using Gaussian deconvolution method. The peaks of Ce 3*d* and O 1s orbitals for the four samples are shown in Fig. S14 and S15, respectively. The red filled areas represent the density of Ce^{3+} states. The atomic percentages of $[V_O^{\bullet\bullet}]$, derived from Ce^{3+} related peak are 15, 19, 16, and 11 for holey 2D nanosheet, hollow octahedron, hollow sphere and leaf CeO_{2-x} structures, respectively.

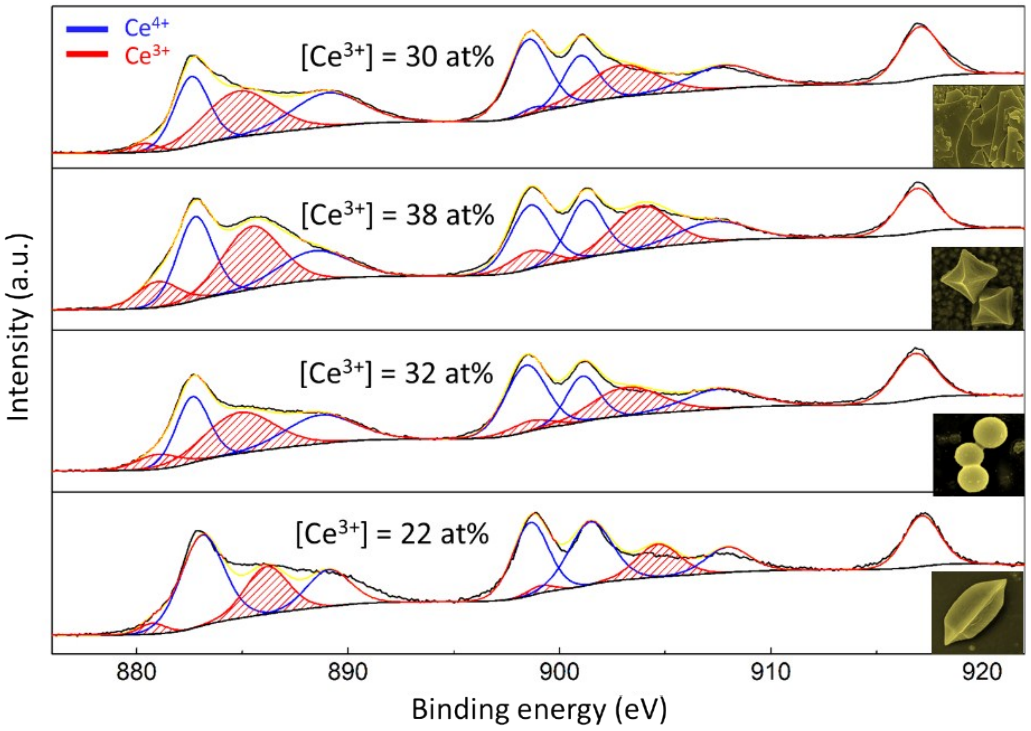

Fig. S14 XPS Ce 3*d* spectra for holey nanosheet, hollow octahedron, hollow sphere, and leaf CeO_{2-x}.

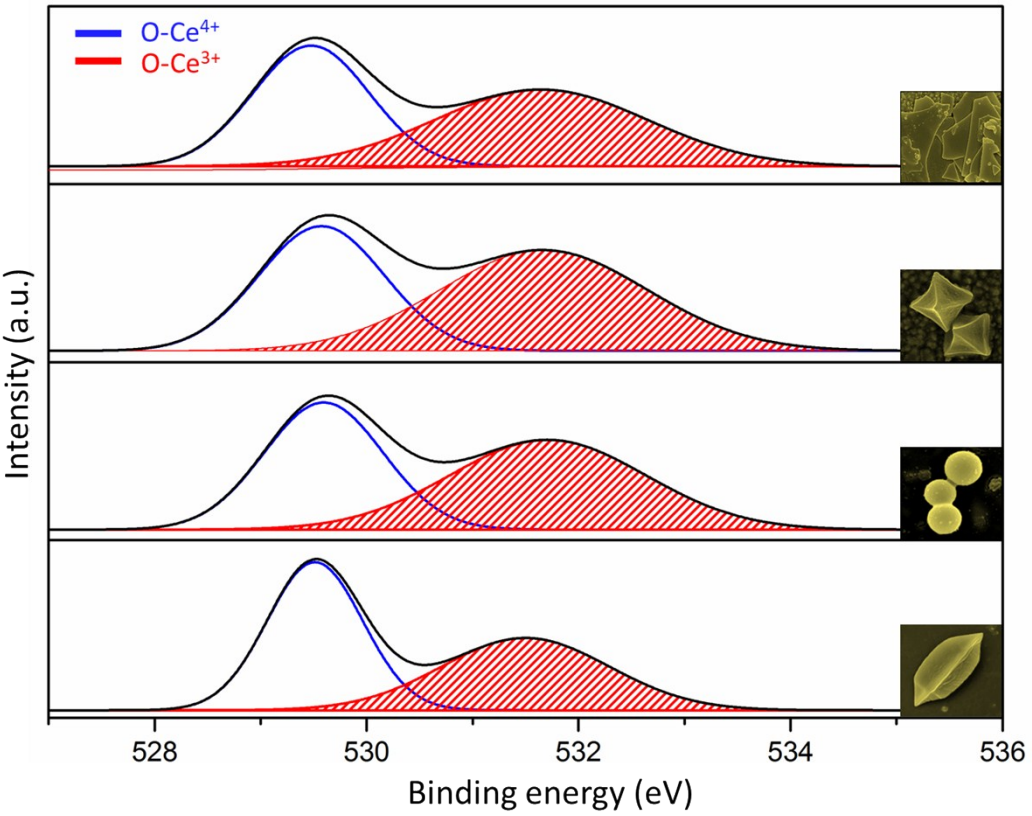

Fig. S15 XPS O 1*s* spectra for holey nanosheet, hollow octahedron, hollow sphere, and leaf CeO_{2-x}.

Table S1 Comparison of MB degradation performance for holey CeO_{2-x} reported

Material	Morphology	CeO_2 crystallite size (nm)	[Dye] (mol L^{-1})	Solids loading (mg mL^{-1})	Radiation source	Degradation for 2 h (%)[A]	Specific surface area (m^2/g)	Pore size (nm)/ pore volume ($cm^3\ g^{-1}$)	Kinetics (min^{-1})	$[V_O^{\bullet\bullet}]$ (at %)	Ref.
CeO_2	Anhedron	13	15.00×10^{-6}	1.0	Sunlight	3.9	?	?	?	?	[9]
CeO_2-V_2O_5	Anhedron	11	15.00×10^{-6}	1.0	Sunlight	30.1	?	?	?	?	[9]
CeO_2	Anhedron	8	5.00×10^{-7}	1.0	Sunlight	~32 (50 min)	?	?	?	?	[10]
CeO_2-CuO	Anhedron	9	15.00×10^{-6}	1.0	Sunlight	34.3	?	?	?	?	[9]
CeO_2-ZnO	Anhedron	~10	8.00×10^{-7}	1.0	Simulated Solar light	~51	?	?	?	?	[11]
CeO_2	Anhedron	11	5.00×10^{-4}	2.0	Simulated Solar light	60 (50 min)	?	?	?	?	[12]
CeO_2	Anhedron	~11	?	?	Simulated Solar light	~64	?	?	0.012	?	[13]
CeO_2	Anhedron	~11	?	?	Simulated Solar light	~48	?	3.0/0.104	?	?	[14]
CeO_2-ZrO_2	Anhedron	18.5	?	?	Simulated Solar light	~60	34.30	3.0/0.104	?	?	[14]
CeO_2-ZrO_2	3D porous	~11	?	?	Simulated Solar light	~64	65.40	3.0-36.0/0.48	?	?	[14]

Material	Morphology	CeO_2 crystallite size (nm)	[Dye] (mol L^{-1})	Solids loading (mg mL^{-1})	Radiation source	Degradation for 2 h (%)[A]	Specific surface area (m^2/g)	Pore size (nm)/ pore volume ($cm^3\ g^{-1}$)	Kinetics (min^{-1})	$[V_O^{\bullet\bullet}]$ (at %)	Ref.
CeO_2	Octahedron	~22	6.00×10^{-7}	0.1	Visible light	11	40.84	?	?	~13	[15]
kGy modifgied-CeO_2	Octahedron	~22	6.00×10^{-7}	0.1	Visible light	23	49.63	?	?	~17	[15]
CeO_2	Sphere	?[B]	2.50×10^{-6}	0.4	Visible light	20 (1 h)	2.10	?	0.003	?	[16]
CeO_2-RGO[C]	Octahedron-NS[D]	~12	4.00×10^{-7}	0.1	Visible light	58	40.84	?	?	<10	[17]
CeO_2-RGO	NP[E]-NS	8	5.00×10^{-7}	1.0	Simulated Solar light	~70 (50 min)	?	?	?	?	[10]
CeO_{2-x}	Leaf	4-8[F]	1.00×10^{-6}	0.3	Simulated Solar light	~14	6.3	6.3/0.001		11	Present Work
CeO_{2-x}	Hollow sphere	4-8[G]	1.00×10^{-6}	0.3	Simulated Solar light	~37	53.4	8.0/0.150		16	Present Work
CeO_{2-x}	Hollow octahedron	4-8[H]	1.00×10^{-6}	0.3	Simulated Solar light	~50	47.2	6.8/0.420		19	Present Work
CeO_{2-x}	Holey NS	4-8[I]	1.00×10^{-6}	0.3	Simulated Solar light	~77	80.9	7.4/0.320	0.014	15	Present Work

[A] Unless otherwise noted
[B] Sphere diameter 40 nm
[C] RGO = reduced graphene oxide
[D] NS = nanosheet
[E] NP = nanoparticle
[F] Cross section = ~2-3 µm
[G] Diameter = ~400 nm
[H] Cross section ~1 µm
[I] Thickness range ~15-100 nm

Table S2 Effects of concentration, temperature, and vapour pressure (ideal gas) on morphological variations of Ce-CP.

Concentration (M)	Temperature (˚C)	Vapour Pressure (kPa)	Nanostructure
4	–10	0.744	Thin Nanosheet
8			
4	0	1.568	Thick Nanosheet
16			Hollow Sphere
4	+25	7.830	Hollow Sphere
8			Hollow Pseudoctahedron
40			Hollow Elongated Octahedron
120			Solid Leaf

References

1. N. Kanagathara, N. G. Renganathan, M. K. Marchewka, N. Sivakumar, K. Gayathri, P. Krishnan, S. Gunasekaran and G. Anbalagan, *Spectrochimica acta. Part A, Molecular and biomolecular spectroscopy*, 2013, **101**, 112-118.
2. N. Kanagathara, N. G. Renganathan, M. K. Marchewka, N. Sivakumar, K. Gayathri, P. Krishnan, S. Gunasekaran and G. Anbalagan, *Spectrochimica Acta Part A: Molecular and Biomolecular Spectroscopy*, 2013, **101**, 112-118.
3. E. Spinner, *Journal of the Chemical Society (Resumed)*, 1964, DOI: 10.1039/JR9640004217, 4217-4226.
4. D. A. Long, *J. Raman Spectrosc.*, 2004, **35**, 905-905.
5. A. C. Cabral, L. S. Cavalcante, R. C. Deus, E. Longo, A. Z. Simões and F. Moura, *Ceramics International*, 2014, **40**, 4445-4453.
6. *Journal of Raman Spectroscopy*, 1992, **23**, 267-272.
7. V. N. Krishnamurthy and S. Soundararajan, *Journal of the Less Common Metals*, 1967, **13**, 263-268.
8. S. S. Mofarah, E. Adabifiroozjaei, R. Pardehkhorram, M. H. N. Assadi, M. Hinterstein, Y. Yao, X. Liu, M. B. Ghasemian, K. Kalantar-Zadeh, R. Mehmood, C. Cazorla, R. Shahmiri, G. Bahmanrokh, S. Bhattacharyya, M. Chiara Spadaro, J. Arbiol, S. Lim, Y. Xu, H. Arandiyan, J. Scott, P. Koshy, and C. C. Sorrell, Advanced Materials, 2019, 1905288.
9. R. Saravanan, S. Joicy, V. K. Gupta, V. Narayanan and A. Stephen, *Materials Science and Engineering. C, Materials for Biological Applications*, 2013, **33**, 4725-4731.
10. S. Kumar and A. Kumar, *Materials Science and Engineering: B*, 2017, **223**, 98-108.
11. R. Manimozhi, D. Ranjith Kumar and A. P. Gnana Prakash, *Journal of Electronic Materials*, 2018, **47**, 6716-6721.
12. V. Ramasamy, V. Mohana and V. Rajendran, *OpenNano*, 2018, **3**, 38-47.
13. M. K. Chinnu, P. Anandan, M. Arivanandhan, A. Venkatesan, R. M. Kumar and R. Jayavel, *Journal of Materials Science: Materials in Electronics*, 2018, **29**, 9564-9572.
14. Y. Hao, L. Li, J. Zhang, H. Luo, X. Zhang and E. Chen, *International Journal of Hydrogen Energy*, 2017, **42**, 5916-5929.
15. M. M. Khan, S. A. Ansari, D. Pradhan, D. H. Han, J. Lee and M. H. Cho, *Industrial & Engineering Chemistry Research*, 2014, **53**, 9754-9763.
16. Z.-M. Yang, G.-F. Huang, W.-Q. Huang, J.-M. Wei, X.-G. Yan, Y.-Y. Liu, C. Jiao, Z. Wan and A. Pan, *J. Mater. Chem. A*, 2014, **2**, 1750-1756.
17. M. E. Khan, M. M. Khan and M. H. Cho, *Sci Rep*, 2017, **7**, 5928.